Development and validation of the higher-order finite-difference wind farm simulator, WInc3D

G. Deskos & M. D. Piggott
Department of Earth Science and Engineering, Imperial College London, London, UK

S. Laizet
Department of Aeronautics, Imperial College London, London, UK

ABSTRACT: High-fidelity wind farm models typically employ large–eddy simulation (LES) formulations and turbine parametrisations (e.g. actuator disc models) to resolve the turbine wakes at spatial and temporal scales so that all flow features of engineering improtance are well–captured. Such features include the low frequency dynamic wake meandering, which plays a key role in the fatigue loading experienced by downstream turbines clustered in arrays. By the term 'wind farm simulator' (WFS) we refer to an integrated framework which offers these capabilities and can be used as a research tool to study wake–to–wake and turbine–to–wake interactions. In this work, we present a validation study for `WInc3D`, a WFS based on the powerful, sixth-order finite-difference flow solver, `incompact3d`. For our validation study, we use operational scenarios from the Horns Rev offshore wind farm. The comparison of the present model with existing supervisory control and data acquisition (SCADA) measurements and previous LES studies shows an overall good agreement.

1 INTRODUCTION

Modern large–scale offshore wind farms consist of multiple turbines clustered together usually in well–structured formations (e.g. Lillgrund, Horns Rev, Nysted). Such a clustering exhibits a number of drawbacks during the operation of the wind farm, as some of the downstream turbines will inevitably have to operate within the wake of the upstream ones. A wind turbine operating within a wake field is an issue for two reasons. First, the apparent reduction of its power output due to the wind speed de–acceleration and second an increase of the fatigue loads due to experiencing the upstream wake–laden turbulence. Power losses due to wake effects were recently reported to be in the order of 10–25 $\%$ (Barthelmie et al. 2009, Barthelmie and Jensen 2010) while the fatigue–related failures were reported to be around the same levels owing to a limited understanding of the offshore turbulence (Wang et al. 2014). With this in mind, it is evident that a wind farm wake model, which can predict both wake deficits and unsteady loads on the individual turbines, with high accuracy is a necessity. Existing wake models span from empirical and semi–empirical models (Jensen 1983, Ainslie 1988) to dynamic stochastic models (Larsen et al. 2007) or more computationally expensive models which solve the Navier-Stokes equations to a desired temporal and spatial scale. The latter category of models is becoming more popular, as high performance computing (HPC) platforms are becoming more powerful and capable of affording larger sized computational problems. In that respect, the use of high–order numerical schemes and fast computational algorithms that take advantage of modern hardware architectures are key to further boosting the computational efficiency of the numerical algorithms.

To this day, a number of wind farm simulators (WFS) exist which offer a number of modelling options, including modelling the ambient atmospheric flow conditions, various turbine parametrisations (e.g. actuator disc (AD), actuator line (AL) or actuator surface (AS) models) as well as active control either on a turbine or plant level. The ability of a WFS to accurately capture complex flow dynamics of utility–scale wind farms has been demonstrated by Churchfield et al. (2012) and Nilsson et al. (2015) for the Lillgrund offshore wind farm, and Wu and Porté-Agel (2015) for the Horns Rev wind farm, while a number of other wind farm simulations have been undertaken for theoretical wind farm layouts (Wu and Porté-Agel 2013, Chatterjee and Peet 2018) to assess the impact of micro–siting (amongst other effects). More recently, the idea of using a plant–level optimal control strategy with large–eddy simulations was proposed by (Munters and Meyers 2017). They found that the op-

timal control strategy (cooperative) yielded a cumulative 16% increase for the power output compared to the turbine–controlled (greedy) case. These studies and other similar works which grow in number show the potential of wind farm simulators to become a useful tool in providing high–fidelity data for design and control purposes.

In this work, we present a validation for `WInc3D`, an open–source wind farm simulator based on higher–order finite–difference discretisation schemes. The paper starts with a short description of the numerical solver including the boundary conditions and wall-stress model in section 2 and the actuator line model and its active controller in section 3. The model validation against SCADA data and previous LES simulations is presented in section 4 by considering flow scenarios from the Horns Rev offshore wind farm. Finally, conclusions and future development directions of the code are presented in sections 5 and 6, respectively.

2 NUMERICAL SOLVER

The present numerical model solves the unsteady incompressible Navier–Stokes equations,

$$\frac{\partial u_i}{\partial t} + \frac{1}{2}\left(u_j \frac{\partial u_i}{\partial x_j} + \frac{\partial u_i u_j}{\partial x_j} \right) = -\frac{1}{\rho}\frac{\partial p}{\partial x_i} - \frac{\partial \tau_{ij}}{\partial x_j} + \frac{F_i}{\rho}, \tag{1}$$

$$\frac{\partial u_i}{\partial x_i} = 0, \tag{2}$$

where $p(x_j,t)$ and $u_i(x_j,t)$ are the large–scale components of the pressure and velocity fields, respectively, obtained through the numerically obtained scale separation based on the grid size Δ, and ρ the fluid density which is taken equal to unity. The two other right–hand side terms, $-\partial_j \tau_{ij}$ and F_i/ρ are the subgrid–scale (SGS) momentum flux and the body forcing, respectively. The SGS stress tensor τ_{ij} is calculated using the standard Smagorinsky model (Smagorinsky 1963)

$$\tau_{ij} = -2(C_S\Delta)^2 |S| S_{ij}, \tag{3}$$

where

$$S_{ij} = \frac{1}{2}\left(\frac{\partial u_i}{\partial x_j} + \frac{\partial u_j}{\partial x_i} \right), \tag{4}$$

is the strain rate, $|S|$ its magnitude, C_S is the Smagorinsky constant and Δ the grid size taken equal to $\Delta = \sqrt[3]{\Delta x \Delta y \Delta z}$. On the other hand, the body force F_i can be considered to have a double use. First, during the precursor simulations, F_i is given a constant value of $\rho u_*^2/\delta$, where δ is the height of the boundary layer in order to force the atmospheric boundary layer (ABL) to a particular condition (e.g. to give geostrophic forcing) and secondly, during the wind farm simulations to represent the turbine source term. The procedure that is followed for calculating the turbine momentum source will be discussed in more detail in section 3. The underlying fluid solver is build upon the open–source code `incompact3d` (Laizet & Lamballais 2009) which has been applied to a variety of problems and provides multiple options for the numerical solver and/or the turbulence modelling (e.g. DNS, explicit LES, implicit LES). The particular numerical solver which is utilised within `WInc3D` however, descritises equations (1) and (2) with the aid of sixth–order accurate compact finite difference schemes for the spatial derivatives and an explicit third–order Runge–Kutta scheme for the temporal ones. The solver uses a Cartesian mesh in a half-staggered arrangement – a different mesh is used only for pressure p – and a direct Poisson solver is used to solve for the pressure field. The code is parallelised with the aid of MPI and an efficient 2D pencil domain decomposition (Laizet and Li 2011).

2.1 *Boundary conditions and the rough–wall shear stress model*

The wind farm simulations are considered in a (x, y, z) coordinate system with the y axis corresponding to the vertical direction as shown in figure 1. For the presented simulations, we will assume periodic and inflow/outflow conditions in the x–direction for the precursor and full simulations, respectively, periodic boundary conditions for the transverse direction, a stress-free $\partial_{x,z} u_i = u_y = 0$ for $i \in \{x,z\}$ on the upper wall (lid) and a rough wall stress model on the bottom of the domain. Here we make use of the wall stress model of Moeng (1984) which relates the instantaneous shear stresses with the plane–average and instantaneous velocities via

$$\tau_{iy} = -u_*^2 \frac{V_{1/2}\langle u_i\rangle_{1/2} + \langle V_{1/2}\rangle((u_i)_{1/2} - \langle u_i\rangle_{1/2})}{\langle V_{1/2}\rangle(\langle u_x\rangle_{1/2}^2 + \langle u_z\rangle_{1/2}^2)^{1/2}} \tag{5}$$

where the subscript $1/2$ denotes the value obtained at the middle distance between the first and second grid levels from the wall, $V_{1/2} = \sqrt{(u_x)_{1/2}^2 + (u_z)_{1/2}^2}$ being the magnitude of the horizontal velocity at the $1/2$ location, $\langle \cdots \rangle$ a spatial average taken over the horizontal plane and u_* is the friction velocity computed at each time step via

$$u_* = \frac{\kappa}{\ln(y_{1/2}/y_0)} \sqrt{\langle u_x\rangle_{1/2}^2 + \langle u_z\rangle_{1/2}^2}, \tag{6}$$

where κ is the von Kármán constant and y_0 the roughness length scale. In addition, in order to address the surface layer mismatch owning to the excessive dissipative action of the Smagorinsky model we make

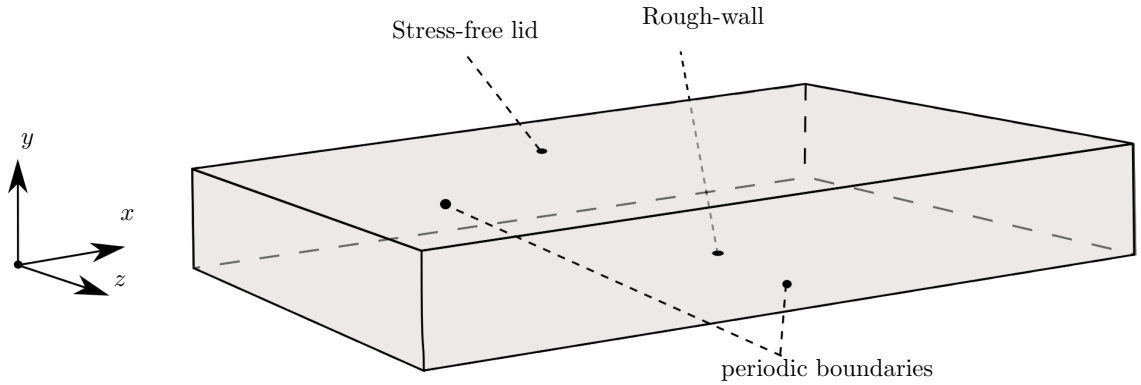

Figure 1: Schematic representation of the computational domain.

use of the damping function proposed by Mason & Thomson (1992),

$$C_S = \left(C_0^{-n} + \left\{ \kappa \left(\frac{y}{\Delta} + \frac{y_0}{\Delta} \right) \right\}^{-n} \right)^{-1/n}, \tag{7}$$

and choose $C_0 = 0.2$ and $n = 1$. The validity of this choice will be further discussed in the context of the produced first and second order statistics (streamwise mean velocity $\langle U_x \rangle$ and turbulence intensity $\mathcal{I}$). We should also stress that on both the bottom and top (lid) walls, the no-penetration condition is enforced using anti–symmetric boundary conditions for u_y, $u_y(-y) = -u_y(y)$ and $u_y(0) = 0$, by considering ghost cells extending outside the computational domain. This set of boundary conditions, in combination with a skew-symmetric formulation of the convective term was also advocated by Xie et al. (2015) to yield better results for a nearly-neutral atmospheric boundary layer.

3 ACTUATOR LINE MODEL

In large–scale wind farm simulations, it has been a common practice to represent the wind turbines via low–order parametrisation models, in an attempt to reduce the computational complexities and resources associated with resolving the boundary layer of individual blades. Thus, actuator disc, line or even surface models have long been used and advocated as parametrisation models for the turbine forcing term added to the fluid solver. `WInc3D` utilises the actuator line model (ALM) of Sørensen and Shen (2002) and combines it with a number of additional models (tip loss correction, dynamic stall, and dynamic tower forcing) to account for the dynamic effects/response of the wind turbines to unsteady loading.

3.1 *Blade aerodynamics*

Our particular ALM formulation involves the use of both a standard and a dynamic procedure for calculating the blade forces. Starting with the former, the standard procedure makes use of tabulated steady state airfoil coefficients such as the lift C_L and drag C_D to calculate the forces. First the blade-element local normal and tangential velocities (combined with the relative velocity of the structure) u_n, u_t are extracted from the fluid solver and used to calculate the velocity magnitude $u_r = \sqrt{u_n^2 + u_t^2}$ and the local angle of attack $\alpha = \tan^{-1}(u_r/u_t)$. The angle of attack is used by the look-up procedure to find the corresponding aerodynamic coefficient (C_L, C_D), convert them to the respective normal and tangential coefficients C_n, C_t and use them together with the local velocity magnitude to calculate the local blade element forces

$$\mathbf{f}_{\text{blade}} = (f_n, f_t) = \frac{1}{2} \rho c u_r^2 (C_n \mathbf{e}_n + C_t \mathbf{e}_t), \tag{8}$$

where c is the local chord size and $\mathbf{e}_n$, $\mathbf{e}_t$ are the normal and tangential unit vectors of the blade element. In the dynamic procedure the interpolation step for calculating the normal and tangential coefficients is no longer needed. Instead, the coefficients are calculated by separating the aerodynamic response of the airfoil into two phases, a pre– and a post–stall one. The dynamic module for calculating the coefficient is based on the dynamic stall model of Leishman and Beddoes (1989) and its low Mach number modification by Sheng et al. (2008). The aerodynamic coefficients are calculated via an attached/separated flow procedure and a leading–edge vortex model which are used to approximate the dynamic stall for each individual blade element. Further information on the dynamic stall model can be found in Sheng et al. (2008). Once the coefficients have been computed, equation (8) is subsequently used for the forces. Lastly, the calculated actuator line point forces are projected to the fluid mesh using a standard Gaussian smoothing kernel:

$$\mathbf{F}^i_{\text{fluid}} = - \sum_{j=1}^{N_{\text{elements}}} \frac{1}{\epsilon^3 \pi^{3/2}} \exp \left[- \left(\frac{d_{ij}}{\epsilon} \right)^2 \right] \mathbf{f}^j_{\text{blade}}, \tag{9}$$

where d_{ij} is the distance between an actuator line node j and the mesh node i where the forces are projected. The smoothing parameter ϵ is considered constant and equal to $\epsilon = 2.2\Delta$.

3.2 *Active control strategy*

Within `WInc3D` the turbines are controlled via a closed–loop active controller using the "five-regions" approach of Jonkman et al. (2009). The five regions: 1, 1 ½, 2, 2 ½ and 3 as shown in figure 2 below. Re-

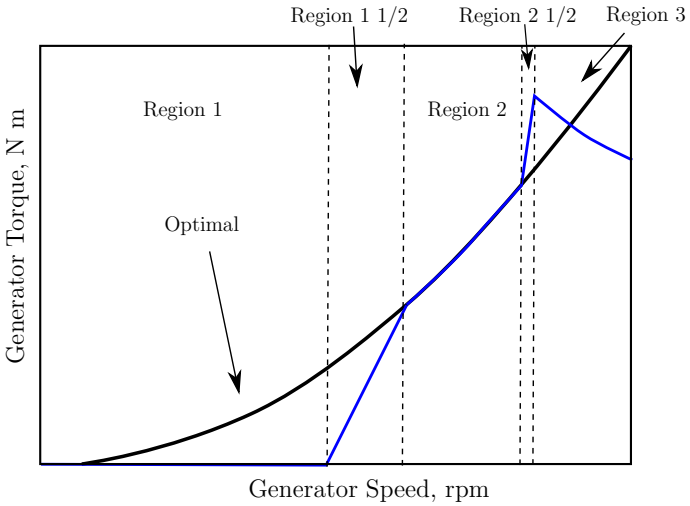

Figure 2: Schematic representation of the "five regions" controller.

gion 1 is the control region before the cut–in speed and the generator torque is considered to be zero and therefore no power is extracted from the wind. Region 2 is a control region which optimises the power output and it is considered to be the desirable state for the turbine. In region 2, the generator torque is proportional to the square of the filtered generator speed $T_{\text{Gen}} = K_2 \Omega_{\text{Gen}}^2$, where K_2 is a constant calculated by taking into account the optimum power coefficient C_P of the turbine. Finally, in region 3 the generator power is held constant and therefore the generator torque is inversely proportional to the filtered generator speed, $T_{\text{Gen}} = K_3 / \Omega_{\text{Gen}}$. Regions 1 ½ and 2 ½ are considered to be linear transitions between Region 1 and 2 and Region 2 and 3, respectively. The first is considered so it can place a lower limit to the generator's speed range while the second an upper limit before entering the "rated power" region. Typically, pitch control will be invoked in Region 3. To relate the generated low–speed (shaft) torque, to the generator torque a number of calculations need to be undertaken, starting with the consideration that the produced shaft torque is equal to

$$T_{\text{shaft}} - N_{\text{GearBox}} T_{\text{Gen}} = (I_{\text{Rotor}} + N_{\text{GearBox}}^2 I_{\text{Gen}}) \frac{d\Omega_{\text{shaft}}}{dt}, \tag{10}$$

where N_{GearBox} is the high–speed to the low–speed gear box ratio, I_{Rotor}, I_{Gen} are the moments of inertia of the rotor and the generator respectively, and Ω_{shaft} the desired optimal low–speed rotational speed of the wind turbine. The procedure for calculating Ω_{shaft} starts with an initial guess, and subsequently the shaft and generator torques are calculated to update it.

4 SIMULATIONS OF THE HORNS REV OFFSHORE WIND FARM

The Horns Rev offshore wind farm is located in the Danish western coast, covering an area of approximately 20 km^2. The farm consists of 80 Vestas V-80 2MW wind turbines each turbine having a rotor diameter $D = 80$ m and a hub height $H_{\text{hub}} = 70$ m. These are distributed in an 8×10 structured grid with a basic spacing of 7 diameters as shown in figure 3. On the site, there are also three masts (M3, M6, M7) which were used to record meteorological measurements (Jensen 2004). Flow conditions in the area are characterised by low turbulence intensity $\mathcal{I} < 8\%$ (Barthelmie et al. 2009) and the atmospheric boundary layer remains at a nearly-neutral stable condition for the majority of the operational hours. The wind resource is dominated by the westerly winds, particularly from the west 270° sector. The westerly wind scenario also makes up the most interesting case scenario for both the power production and mechanical loads as the turbine spacing attains its lowest value ($7D$). In this validation study, we shall consider this flow scenario with deviations of $\pm 1°$, $\pm 5°$ $\pm 10°$ and $\pm 15°$ and the produced normalised power predictions will then be compared with the SCADA data presented by Barthelmie et al. (2009).

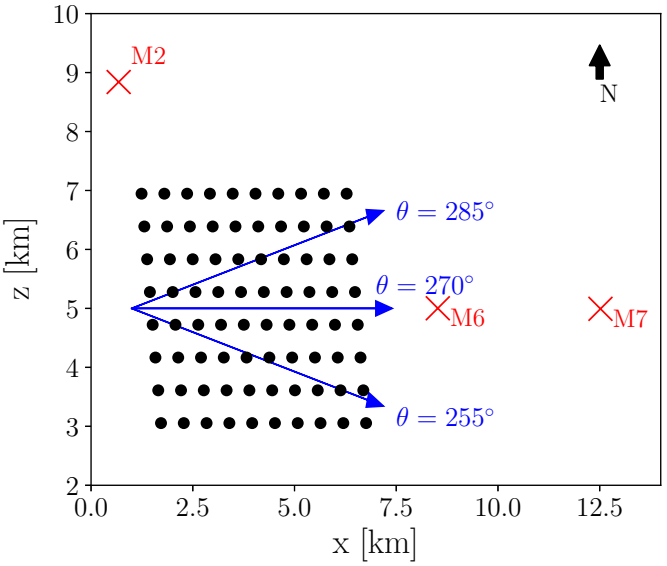

Figure 3: Layout of the Horns Rev wind farm.

4.1 *Precursor simulations*

To obtain an accurate description of the inflow conditions (mean velocity and turbulence intensity) that the Horns Rev wind farm will experience, a precursor simulation needs to be undertaken. Although precursor simulations are much more computationally expensive than the alternative synthetic methods (e.g.

the Mann model, Mann (1998)), they remain a preferred option as they exhibit a number of advantages such as the ability to maintain the large–scale streaky flow structures near the bottom of the boundary layer (Munters et al. 2016). Here, the precursor simulations are undertaken in two steps. First a simulation is run with a large time step (required by the stability conditions of the underlying mesh) for the time that is required until we obtain quasi-stationary turbulence statistics. This requires the use of periodic (cyclic) boundary conditions in the lateral directions (x and z). At the end of the simulations, statistics from the precursor simulation (1) are collected and their accuracy is confirmed by checking the first and second-order statistics (mean velocity and turbulence intensity). The second precursor simulation (2), is subsequently conducted using the final solution (velocity and pressure fields) from the first precursor simulation as an initial condition, by using exactly the same mesh but a smaller time step which this time is determined by the turbine model. This is also the time step to be used in the wind farm simulations. During this second precursor simulation, planes are recorded and stored near the end of the computational domain for a specified time period, which correspond to the inlet planes required by the intended wind farm simulation. To minimise the number of outflow/inflow planes, outlet planes are recorded for a shorter time period than that of the actual wind farm simulation, and are subsequently cycled for the rest of the simulation.

In the present study we present simulations using only part of the wind farm. Given the regularity of the wind farm layout, one may argue that the middle 2 rows of the wind farm can be modelled alone using periodic boundary condition in the span–wise direction. This assumption was also made by Ivanell (2009) and proved to be valid for the same wind farm and flow scenarios. Hence, we consider a domain of $6160\,\mathrm{m} \times 1046\,\mathrm{m} \times 1120\,\mathrm{m}$ which corresponds to a domain of $77D \times 13.1D \times 14D$. For the present simulations the domain was discretised using $616 \times 121 \times 120$ mesh nodes which results in a resolution of $10\,\mathrm{m} \times 8.71\,\mathrm{m} \times 9.33\,\mathrm{m}$. In both the precursor and the final wind turbine simulations the boundary layer is generated with the aid of the wall-shear stress model discussed in section 2.1 using a friction velocity $u_* = 0.442\,\mathrm{m\,s^{-1}}$, a roughness length $y_0 = 0.05\,\mathrm{m}$ and a boundary layer height $\delta = 500\,\mathrm{m}$. The first precursor simulation was run for 200 000 time steps using a time step equal to $\Delta t = 0.1\,\mathrm{s}$ which resulted in 5.5 h of actual time. Snapshots from the precursor simulation are taken at the final time step and shown in figure 4. The three presented snapshots correspond to planes from all three directions (x, y and z) and show the instantaneous stream-wise velocity field. Notice, that the y–plane snapshot is taken at the hub height of the turbines and that it clearly shows a fully developed turbulent field and that large–scale structures are present. From the first precursor simulation we also extract the flow statistics which are collected during the last 100 000 time steps. These are shown in figure 5 where it can be easily seen that the mean–velocity profile follows the logarithmic law and shows excellent agreement near the lower part of the boundary layer where the wind turbines will be located. In addition the computed turbulent intensity at hub height is found to be equal to $\mathcal{I}_{\text{hub}} = 8.8\%$ which agrees well with the value reported by Hansen et al. (2012). Given the good agreement of the flow statistics with the reference data a second precursor simulation was run using a time step of $\Delta t = 0.05\,\mathrm{s}$ for 12 000 time steps (which equals 10 min of actual time) and planes where recorded at a location of one rotor diameter before the end of the domain. These planes, are saved in order to be used as inflow conditions.

4.2 *Turbine parametrisation*

Information of the Vestas V-80 2MW wind turbine is limited and the exact blade design or controller are not fully disclosed. However, a variety of information is available to us via the reports of Jensen (2004) and Ilinca (2011). Amongst the known turbine specification are the rotor diameter $D = 80\,\mathrm{m}$, the hub height $H_{\text{hub}} = 70\,\mathrm{m}$, the airfoil profile "families" (NACA 63-xxx, FFA W3-xxx), the chord size and twist angle at the tip and the root of the blade, as well as the power and thrust coefficient curves as a function of the wind speed. Additional information was also found for the cut-in ($4\,\mathrm{m\,s^{-1}}$) and cut-out $16\,\mathrm{m\,s^{-1}}$) operational wind speeds and rated generator speed. Despite all these, to parametrise the Vestas V-80 2MW turbines we make use of a downscaled version of the NREL 5 MW prototype turbine (Jonkman et al. 2009) and the available information to calibrate the model. A similar, approach was considered by Nilsson et al. (2015) for an actuator disc model. Nevertheless, to validate our assumed parameters we present in figure 6 the model estimates for the power production as a function of the incident wind speed together with the available manufacturers reference data, where it is evident that the downscaling provides an accurate description for all five "regions" of operation.

4.3 *Wind Flow Scenarios*

Having established the validity of the inflow conditions that the wind farm will experience as well as of the turbine parametrisations, we proceed with examining the ability of `WInc3D` to predict the power losses along a row of turbines. For that, we have selected the western mean wind direction $\theta = 270°$ and four wind sector $\pm 1°$, $\pm 5°$, $\pm 10°$ and $\pm 15°$. This scenario has been selected on the basis that in this wind direction the turbines are set in a nearly collocated layout with a horizontal spacing of 7D for the

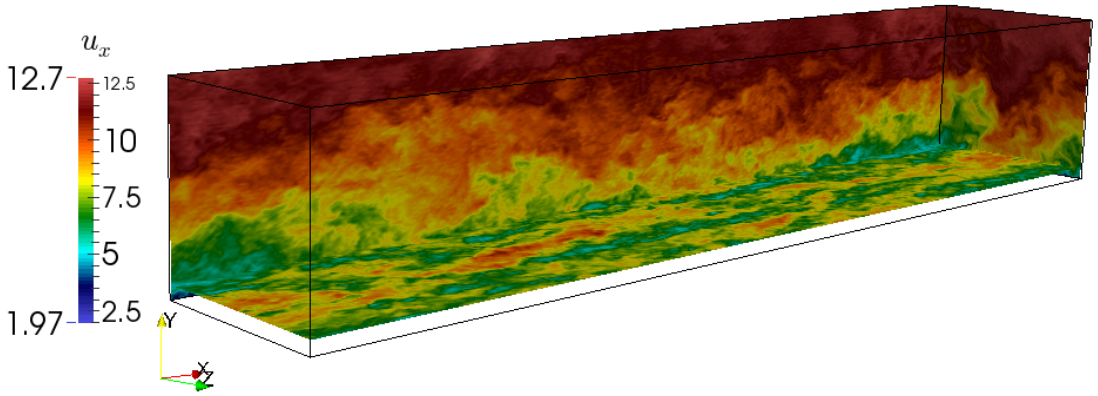

Figure 4: Snapshots taken at the end of the precursor simulation.

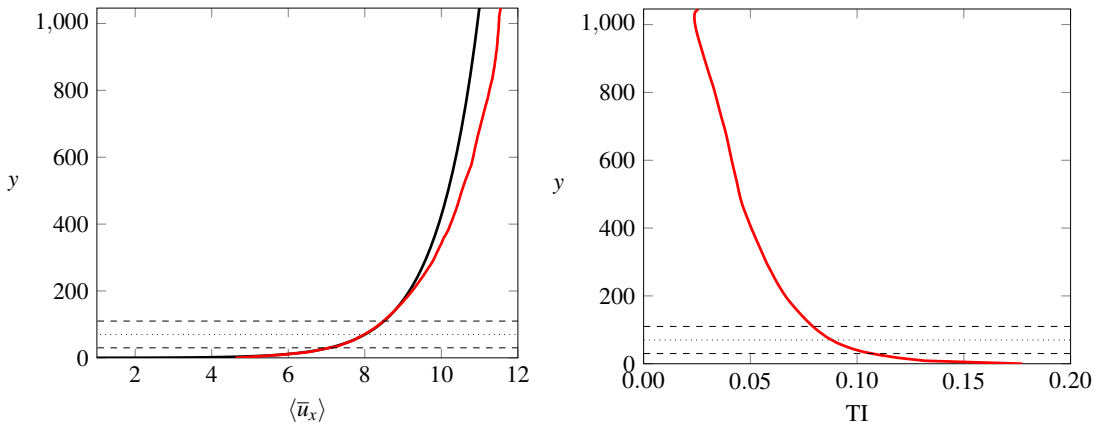

Figure 5: Vertical profiles of the spatial and temporal averages of (a) the stream-wise velocity $\langle \overline{u}_x \rangle$ (red line) and (b) turbulence intensity $\mathcal{I}$ (red line). The solid black line in (a) corresponds to the logarithmic profile. The dashed and dotted lines in both (a) and (b) correspond to the rotor limits and hub height respectively.

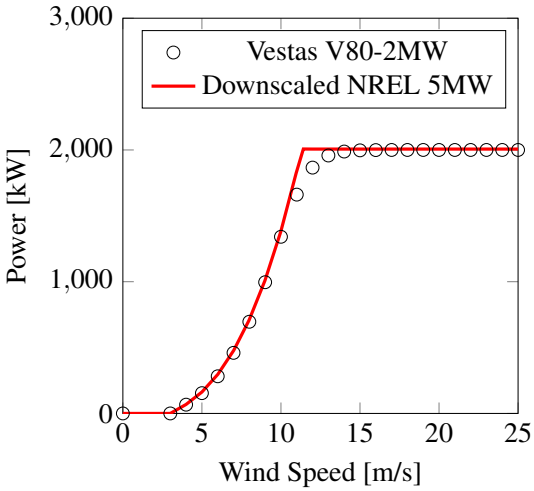

Figure 6: Manufacturer's curve for the Vestas V80-2MW turbine and model predictions based on a downscaled version of the NREL 5MW turbine.

wind sectors $\pm 1°$ and $\pm 5°$. These two cases correspond to the largest reductions in the wake velocities and therefore also the largest power reduction of the downstream turbines. On the other hand, for larger departures (e.g. $\pm 10°$ or $\pm 15°$) the downstream turbines are no longer exposed to the full–wake, thus increasing their power output. This is confirmed by the data presented in figure 7 where the normalised power from the present model, the LES simulations of Wu and Porté-Agel (2015) and the SCADA data of Barthelmie et al. (2009) are plotted for each sector and for each turbine along a row. We should notice

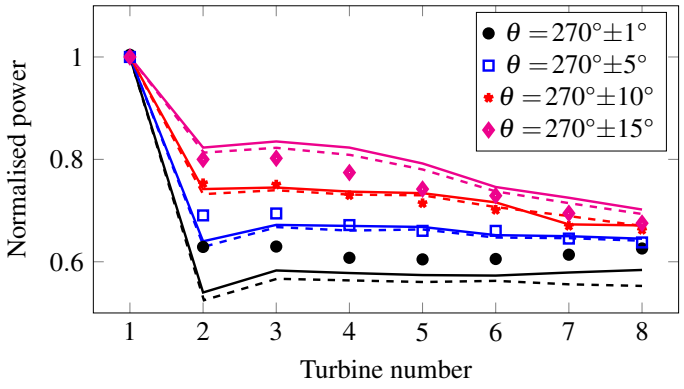

Figure 7: Comparison of the normalised time–averaged power output data. The plot includes the reported SCADA data (symbols), the LES results of Wu and Porté-Agel, 2015 (dashed lines) and the results from the present model (solid lines).

here that the normalised power in our calculations is computed by dividing the time–averaged power output of each turbine with the time–averaged power out-

put of the front turbine and then taking the average of the two simulated rows. The present simulations agree well with both the SCADA data and other LES simulations as shown in figure 7. More specifically, both the present LES results and those of Wu and Porté-Agel (2015) exhibit larger discrepancies compared to the measured data for the wind sectors of $\pm 1^\circ$ and $\pm 5^\circ$. This disagreement can be explained by the fact that for aligned and nearly–aligned turbines, SCADA data are very sensitive to yaw misalignment tracking errors of both the nacelle sensor and the incoming wind direction sensor (Wu and Porté-Agel 2015). This yaw misalignment errors creates an artificially low wake deficit and as a result overpredict the power output along each row. This problem is an endemic uncertainty problem of SCADA measurements (Gaumond et al. 2014) which renders the low angle sectors an unsuitable case for validation. Nevertheless, the present model shows good agreement with both the previous LES results and SCADA data. In particular, our power predictions suffer from the same problems for the near wake profiles although they appear to be able to better predict them, a feature which might be attributed to the superiority of the actuator line model to handle the near–wake field of each turbine. Nevertheless, less variation between the two numerical models and the SCADA data is present for the sectors $\pm 10^\circ$ and $\pm 15^\circ$.

5 CONCLUSIONS

In the present paper, an overview and a validation of the newly developed open–source wind farm simulator `WInc3D`, is presented. The code is built upon the higher–order finite difference numerical solver `incompact3D` which makes use of an efficient 2D domain decomposition algorithm (Laizet and Li 2011) that allows the code to scale on up to $\mathcal{O}(10^5)$ computational cores. In addition, `WInc3D` offers a number of build-in models, including a native actuator line model accompanied with a "five–region" active controller as well as a wall–stress model to simulate a nearly–neutral atmospheric boundary layer. The proposed model offers an alternative tool to both the conventional low–order WFS and the pseudo–spectral based ones currently used in wind energy research. This is due to the fact that the sixth–order compact schemes provide a "spectral–like" accuracy without the restrictions applied by the pseudo–spectral methods.

Here, we present a first attempt towards validating `WInc3D` for full–size wind farm simulations. Previous studies, have used the same code to compare the wake predictions against wind tunnel data (Deskos et al. 2018). For the wind farm validations, we have selected the Horns Rev offshore wind farm, a case for which observed (Barthelmie et al. 2009) and numerical (Ivanell 2009, Wu and Porté-Agel 2015) data exist. From the examination of a single – although, representative of the operational conditions – example, we have demonstrated the ability of `WInc3D` to predict the power losses along a row with high–accuracy. Discrepancies, which are found for the narrowest sectors have been previously observed in the simulations of Wu and Porté-Agel (2015) and discussed by Gaumond et al. (2014). It is however observed that the present model can better estimate the power output for all 4 sectors, a result that might be due to the use of an enhanced actuator line model (see sub-section 3.1) compared to the actuator disc model used by Wu and Porté-Agel (2015). In any case, the examined scenarios cannot be conclusive of the modelling capabilities and therefore, additional simulations would be required.

6 FUTURE WORK

The use of higher–order finite–difference schemes and the 2D pencil domain decomposition makes `WInc3D` a fast and efficient algorithm for high–fidelity simulations of wind farms. However, a number of modelling capabilities are still missing.

These include the introduction of thermal stratification effects which will enable the further study of stable and convective atmospheric boundary layer conditions. In addition, the calculations for the power production and rotor loads of the individual turbines were made without considering the aeroelastic response of the turbine blades. However, given how slender the turbine blades are as well as the existing trend for blades to increase in length, aeroelasticity is undoubtedly one of the central factors affecting the performance and fatigue loading of the individual turbines during their lifespan. In the context of large–scale wind farm simulations aeroelasticity was examined by Churchfield et al. (2012) who showed that the structural response of blades are correlated with the dynamics of the incoming turbulent flow.

Finally, future work will also consider the introduction of plant–level control for the wind farm. The adoption of optimal plant–level control strategies has shown to increase the overall power by more than 27% (Park and Law 2016) when data–driven optimisation algorithms are used. High–fidelity numerical solvers such as `WInc3D` have the ability to generate trustworthy data which can be used to drive these optimisations.

ACKNOWLEDGEMENTS

The authors would like to acknowledge funding from Imperial College London's Energy Futures Lab and the EPSRC (grant number EP/R007470/1). Support for parallel computations was provided by Imperial College's Research Computing Service.

REFERENCES

Ainslie, J. (1988). Calculating the flowfield in the wake of wind turbines. *Journal of Wind Engineering and Industrial Aerodynamics 27*(1), 213 – 224.

Barthelmie, R. J., K. Hansen, S. T. Frandsen, O. Rathmann, J. G. Schepers, W. Schlez, J. Phillips, K. Rados, A. Zervos, E. S. Politis, & P. K. Chaviaropoulos (2009). Modelling and measuring flow and wind turbine wakes in large wind farms offshore. *Wind Energy 12*(5), 431–444.

Barthelmie, R. J. & L. E. Jensen (2010). Evaluation of wind farm efficiency and wind turbine wakes at the nysted offshore wind farm. *Wind Energy 13*(6), 573–586.

Chatterjee, T. & Y. T. Peet (2018). Contribution of large scale coherence to wind turbine power: A large eddy simulation study in periodic wind farms. *Phys. Rev. Fluids 3*, 034601.

Churchfield, M. J., S. Lee, J. Michalakes, & P. J. Moriarty (2012). A numerical study of the effects of atmospheric and wake turbulence on wind turbine dynamics. *Journal of Turbulence 13*, N14.

Churchfield, M. J., S. Lee, P. J. Moriarty, L. A. Martinez, S. Leonardi, G. Vijayakumar, & J. G. Brasseur (2012). A large-eddy simulation of wind-plant aerodynamics. *50th AIAA Aerospace Sciences Meeting Nashville, Tennessee*.

Deskos, G., S. Laizet, & M. D. Piggott (2018). Turbulence-resolving simulations of wind turbine wakes. *arXiv e-prints*. Under review in the Renewable Energy Journal.

Gaumond, M., P. E. Réthoré, O. S., P. A., B. A., & H. K. S. (2014). Evaluation of the wind direction uncertainty and its impact on wake modeling at the horns rev offshore wind farm. *Wind Energy 17*(8).

Hansen, K. S., R. J. Barthelmie, L. E. Jensen, & A. Sommer (2012). The impact of turbulence intensity and atmospheric stability on power deficits due to wind turbine wakes at horns rev wind farm. *Wind Energy 15*(1), 183–196.

Ilinca, A. (2011). Analysis and mitigation of icing effects on wind turbines. In I. H. Al-Bahadly (Ed.), *Wind Turbines*, Chapter 8. Rijeka: InTech.

Ivanell, S. (2009). *Numerical Computations of Wind Turbine Wakes*. Ph. D. thesis, Royal Institute of Technology (KTH).

Jensen, L. (2004). Wake measurements from the horns rev wind farm. In *Proceedings of the European Wind Energy Conference*.

Jensen, N. (1983). *A note on wind generator interaction*.

Jonkman, J., S. Butterfield, W. Musial, & G. Scott (2009). Definition of a 5-mw reference wind turbine for offshore system development. Technical report, National Renewable Energy laboratory.

Laizet, S. & E. Lamballais (2009). High-order compact schemes for incompressible flows: A simple and efficient method with quasi-spectral accuracy. *Journal of Computational Physics 228*(16), 5989 – 6015.

Laizet, S. & N. Li (2011). Incompact3d: A powerful tool to tackle turbulence problems with up to o(105) computational cores. *International Journal for Numerical Methods in Fluids 67*(11), 1735–1757.

Larsen, G. C. A. M. H., F. Bingöl, J. Mann, S. Ott, V. Sørensen, J.N.and Okulov, M. Troldborg, N.and Nielsen, K. Thomsen, T. J. Larsen, & R. Mikkelsen (2007). Dynamic wake meandering modeling. Technical report, TechnicalUniversity of Desnmark.

Leishman, J. G. & T. S. Beddoes (1989). A semi-empirical model for dynamic stall. *Journal of the American Helicopter Society 34*.

Mann, J. (1998). Wind field simulation. *Probabilistic Engineering Mechanics 13*(4), 269 – 282.

Mason, P. J. & D. J. Thomson (1992). Stochastic backscatter in large-eddy simulations of boundary layers. *Journal of Fluid Mechanics 242*, 51 – 78.

Moeng, C.-H. (1984). A large-eddy-simulation model for the study of planetary boundary-layer turbulence. *Journal of the Atmospheric Sciences 41*(13), 2052–2062.

Munters, W., C. Meneveau, & J. Meyers (2016, May). Turbulent inflow precursor method with time-varying direction for large-eddy simulations and applications to wind farms. *Boundary-Layer Meteorology 159*(2), 305–328.

Munters, W. & J. Meyers (2017). An optimal control framework for dynamic induction control of wind farms and their interaction with the atmospheric boundary layer. *Philosophical Transactions of the Royal Society of London A: Mathematical, Physical and Engineering Sciences 375*(2091).

Nilsson, K., S. Ivanell, K. S. Hansen, R. Mikkelsen, J. N. Sørensen, S.-P. Breton, & D. Henningson (2015). Large-eddy simulations of the lillgrund wind farm. *Wind Energy 18*(3), 449–467.

Park, J. & K. H. Law (2016, Sept). Bayesian ascent: A data-driven optimization scheme for real-time control with application to wind farm power maximization. *IEEE Transactions on Control Systems Technology 24*(5), 1655–1668.

Sheng, W., R. A. Galbraith, & F. N. Coton (2008). A modified dynamic stall model for low mach numbers. *Journal of Solar Energy Engineering*.

Smagorinsky, J. (1963). General circulation experiments with the primitive equations. *Monthly Weather Review 91*(3), 99–164.

Sørensen, J. & W. Z. Shen (2002, May). Numerical modeling of wind turbine wakes. *Journal of Fluids Engineering 124*(2), 393–399. 2002.

Wang, H., R. J. Barthelmie, S. C. Pryor, & H. G. Kim (2014). A new turbulence model for offshore wind turbine standards. *Wind Energy 17*(10), 1587–1604.

Wu, Y.-T. & F. Porté-Agel (2013). Simulation of turbulent flow inside and above wind farms: Model validation and layout effects. *Boundary-Layer Meteorology 146*(2), 181–205.

Wu, Y.-T. & F. Porté-Agel (2015). Modeling turbine wakes and power losses within a wind farm using les: An application to the horns rev offshore wind farm. *Renewable Energy 75*, 945 – 955.

Xie, S., N. Ghaisas, & C. L. Archer (2015). Sensitivity issues in finite-difference large-eddy simulations of the atmospheric boundary layer with dynamic subgrid-scale models. *Boundary-Layer Meteorology 157*(3), 421–445.